International Journal of Automotive Technology, Vol. 22, No. 5, pp. 1227–1243 (2021)
DOI 10.1007/s12239–021–0108–1

pISSN 1229–9138/ eISSN 1976–3832

WAKE FLOWS OF HIGHLY DETAILED HEAVY VEHICLES

Damien McArthur, David Burton*, Timothy Crouch, Mark Thompson and John Sheridan

School of Mechanical, Aerospace Engineering, Monash University, Melbourne 3800, Australia

(Received 3 September 2019; Revised 1 June 2020; Accepted 20 July 2020)

ABSTRACT–This work presents a detailed wind tunnel investigation into the nature of the unsteady flow mechanisms that dictate the aerodynamic forces acting on prime-mover trailer heavy vehicles fitted with various passive flow control devices. This work builds on the current understating of the wake flow physics of heavy vehicles that until now has primarily been developed from studies utilising highly simplified geometries or time-averaged findings with realistic geometries. Unsteady base-surface and wake pressure measurements reveal how the time-averaged and unsteady flow field responds to the addition of passive aerodynamic devices that have been shown to be effective on operational heavy vehicles for improving fuel economy and reducing emissions. In comparing turbulent wake statistics and unsteady modes the time-averaged and unsteady flow response is linked directly to the measured changes in the aerodynamic drag coefficient thorough surface pressure and force measurement. The large variation in the wake structure and dynamics observed between test configurations highlights the importance of considering the detailed geometry of heavy vehicles when looking to develop advanced aerodynamic control devices that would provide benefits above and beyond those focused on in this study.

KEY WORDS : Heavy vehicles, Aerodynamic drag, Bluff bodies, Wake flows

1. INTRODUCTION

Fuel usage resulting from the heavy vehicle road transport industry represents both a significant economic cost and a source of polluting emissions. At typical highway speeds, aerodynamic drag is the dominant resistive force on a heavy vehicle. As a result, heavy vehicle drag reduction is an important area of research. The unsteady nature of heavy vehicle wakes has important implications for drag, buffeting of nearby pedestrians and cyclists, and the vehicle's potential receptivity to various active flow control approaches.

A wealth of experimental and numerical data exists on the aerodynamic forces and flow-fields around simplified bluff body heavy vehicle geometries. Simplified bodies retain only the large-scale features of heavy vehicles and include generic square-back, cubic and rectangular prism bodies. Detailed models, which are the focus of this investigation, retain many of the mid-to-small scale features such as wheels and covers, prime-mover features, under-body geometry and corner radii to name a few. Such small-scale features can have a significant impact on heavy vehicle aerodynamics and the effectiveness of flow control devices for reducing fuel consumption. A more complete understanding of flow separation and unsteady wake flow mechanisms for detailed geometries is pivotal to further the aerodynamic fuel efficiency of operational heavy vehicles.

More recent experimental investigations by (McArthur *et al.,* 2016) and (Castelain *et al.,* 2018) presented detailed velocity fields in the wake of the simplified truck models for low Reynolds numbers. However, there is very little information about the wakes of detailed heavy vehicles available in the open literature. Reasons for this include the desire for vehicle and trailer manufacturers to retain a commercial advantage and the cost and difficulty associated with wind tunnel testing of full-sized heavy vehicles. There are examples of published work on full scale (Lanser *et al.,* 1991) and (Leuschen and Cooper, 2006) and larger scale vehicles (Cooper and Leuschen, 2005). However, these studies consider only the aerodynamic drag force to evaluate the aerodynamic performance of add-on passive drag reduction devices with little insight into the drag production and reduction flow mechanisms.

One notable exception to this is the novel setup of (Haff, 2015), who measured on-road base pressure and performed particle image velocimetry (PIV) measurements in the wake of a full scale truck at a Reynolds number of 4×10^6. Wake measurements showed a large scale vortex in the lower part of the vehicle's symmetry plane. This structure is similar to those observed in the wakes of simplified heavy vehicles. Haff also conducted PIV measurements on a 1:15 scale wind tunnel model at a Reynolds number of 6.5×10^5 and noted that the lower vortex was displaced vertically upwards. This was suggested to be likely a results of model geometric simplifications, leading to reduced under-body

*Corresponding author. e-mail: david.burton@monash.edu

blockage compared to the full-scale findings.

There is currently a lack of information addressing the transition in steady and unsteady flow characteristics of a simplified wake to those of a real on-road vehicle. It is not yet clear how the large-scale flow structures identified for simplified reduced scale geometries relate to those in the wakes of detailed heavy vehicles. With the majority of research focusing on modifications to the rear it is also unknown to what extent the wake is affected by modifications to the front of a heavy vehicle.

In this paper we have applied advanced experimental methods and analysis techniques to a large (1:3) scale wind tunnel model that until now have only been reserved for the simplest of analogous heavy vehicle geometries. In doing so we are able to describe how the time-averaged and unsteady flow field responds to the systematic addition of passive aerodynamic devices that have been shown to be effective on operational heavy vehicles for improving fuel economy. Importantly, we are able to link the time-averaged and unsteady flow response directly to the measured changes in the aerodynamic drag coefficient through surface pressure and force measurements. In doing so a strong foundation is formed for maximising the potential of known passive technologies to reduce fuel consumption across a broader range of heavy vehicle geometries and develop advanced technologies, such as active flow control techniques, to perform at a level above and beyond what is currently achievable through commonly used aerodynamic drag minimising practices.

2. METHODOLOGY

2.1. Experimental Facility

Experiments were carried out in the 2.6 m × 4.0 m × 12.0 m test section at the Monash University 1.4 MW 3/4 open jet wind tunnel at a test velocity 'U' of 27 m/s. At the test velocity the boundary layer displacement thickness at the front of the model is 12 mm, which is 14 % of the frontal ground clearance. The mean streamwise turbulence intensity 'Iu' and uniformity in dynamic pressure 'Δq' outside of the boundary layer is 1.6 % and 1.5 % respectively. Wind tunnel test conditions are representative of a low freestream turbulence environment. This type of environment is characteristic of heavy vehicles operating in still winds in the absence of nearby road users.

In order to account for the large blockage 'B' of 10.6 %, a number of modifications were made to the 3/4 open jet test section. Details of the modifications and results of the subsequent flow validation are presented in (McArthur *et al.,* 2016). A summary of the wind tunnel test conditions that were consistent across all measurements undertaken with the detailed 1:3 scale prime-mover trailer model is provided in Table 1.

The origin of the wind tunnel coordinate system for this investigation is the centre of the lower edge of the base of the vehicle. The X-axis is in the downstream direction, the Z-axis is vertically upwards and the Y-axis follows from a conventional orthogonal coordinate system.

Table 1. Wind tunnel test conditions for experiments conducted utilising various instrumentation. The measurement location 'X' represents the number of trailer widths 'W' downstream from the base of the trailer.

	U	Iu	δ^*	Δq	B
Exp. Test Conditions	27 m/s	1.6 %	12 mm	1.5 %	11 %

	X=0	X=1	X=2	X=3
Multi-hole probe (4)	x	x	x	-
Total pressure grid	-	x	x	x
Dyn. surface pressures	x	-	-	-

2.2. Model Geometry

The geometry used for this investigation is a 1:3 scale model, modified from a commercially available Cab-over-Engine (CoE) tractor mated to a commercially available articulated box-trailer. The overall model dimensions are height H = 1,400 mm, width W = 830 mm, length L = 6,000 mm, tractor-trailer gap G = 680 mm and ground clearance at the front of the truck = 83 mm. Details of the model and results of a comprehensive drag reduction program have been published in (McArthur *et al.,* 2013). In this investigation a number of configurations of the CoE model are selected for flow mapping, this is intended to allow characterisation of a range of heavy vehicle wakes, representative of different vehicles currently in operation. Figure 1 depicts the Cab-over-engine geometries selected for this study and the aerodynamic performance of each configuration relative to the baseline model that exhibited the highest aerodynamic drag ΔCd_{Sharp}. The geometries selected in order of decreasing drag coefficient include:

1. The Sharp vehicle is the highest drag model tested and consists of flat top cab in front of a trailer with sharp leading edges.
2. The Flat vehicle also employs the flat top cab. In this configuration the trailer is equipped with rounded leading edges and an external refrigeration unit.
3. The Fairing vehicle incorporates a sleeper cab tractor with a roof fairing and angled side extenders that are 0.165 G long and angled outwards at 15 °. Once again, the trailer is equipped with rounded leading edges and an external refrigeration unit.

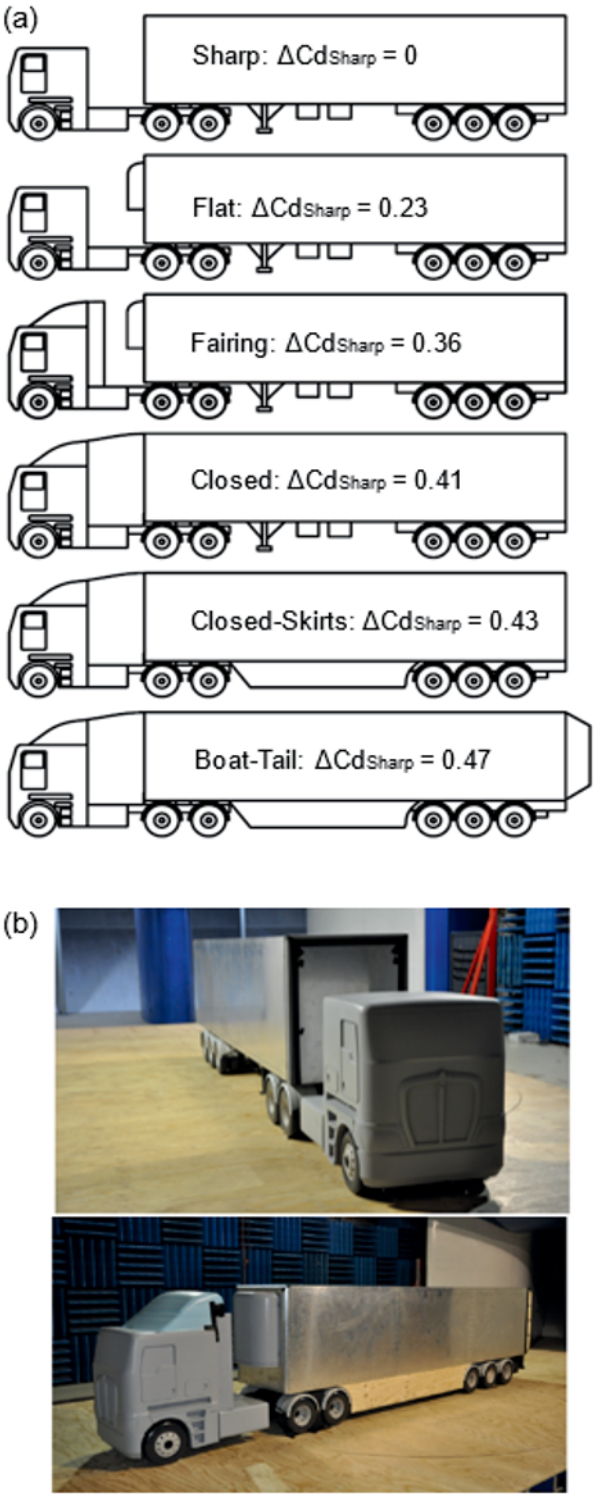

Figure 1. (a) Schematics of model configurations, from top to bottom in order of decreasing drag coefficient: Sharp, Flat, Fairing, Closed, Closed-Skirts, Boat-Tail; (b) Image of the wind tunnel set-up with the detailed 1:3 scaled model in the high-drag sharp vehicle and low-drag boat-tail configuration.

4. The Closed vehicle includes the fairing cab, 1.0 G long side extenders and an additional surface that is sealed from the trailing edge of the roof fairing to the leading edge of the trailer, thus eliminating the tractor-trailer gap.
5. The Closed-Skirts model is the same as the Closed, with the addition of trailer mounted side-skirts that cover 79 % of the trailer ground clearance height.
6. The Boat-Tail model is the same as the Closed-Skirts, with the addition of 0.24 W long boat-tails, placed on the upper and side trailing edges of the vehicle at an angle of 15 °.

The four main front-end configurations chosen reflect not only variations among the range of drag values seen in typical heavy vehicles but also the fundamentally different flow interaction that occur between the cabin and trailer. For the Closed configurations, the cab and trailer are effectively a single body. In this situation the flow stagnates at the front of the vehicle and then the boundary layer develops continuously down the upper and side faces of the truck/trailer.

The Fairing cab is the first of the two-body systems, where flow separates from the tractor and reattaches on the trailer. In this configuration the roof fairing and side extenders serve to shield the trailer from incoming flow so there is not a significant stagnation of flow on the front face of the trailer and the separating shear layer from the cabin joins with the boundary layer along the top and sides of the trailer.

The Flat cab has neither the roof fairing or side extenders. This means less flow is deflected away from the trailer and consequently, more high speed flow interacts with the front face of the trailer. As the front of the trailer has a curved refrigeration unit and rounded leading edges, the boundary layer that begins on the front of the trailer remains attached along these convex surfaces.

The Sharp configuration represents the final category of tandem body aerodynamics, where flow once again interacts with the front face of the trailer, but due to the sharp leading edges, undergoes large-scale separation.

2.3. Measurement Instrumentation

Are range of experimental techniques have been utilised to study the near wake of the detailed heavy vehicle model. A summary of the instrumentation used during near wake experiments and to measure unsteady surface pressures on the base of the trailer is provided in Table 1. Here we define the measurement location downstream of the base of the trailer by the nondimensional parameter ($x^* = \frac{x}{W}$), where 'x' is the downstream distance and W is the width of the trailer. A test matrix summarising experiments performed with these instruments is provided in Table 1.

Wake velocity measurements were obtained using a

4-hole dynamic pressure probe, or cobra probe, manufactured by Turbulent Flow Instrumentation Pty Ltd at a width-based Reynolds number ($Re_W = \frac{U_0 W}{\mu}$) of 1.4×10^6. Multi-hole pressure probes have been successfully used to measure similar turbulent flows. The probe head has four triangular faceted surfaces, each with a 0.5 mm diameter hole in the centre connected to an internal pressure transducer as in (Hooper and Musgrove, 1997). From the relationship between the pressures at each face, the 3 components of velocity (u, v, w) and static pressure can be obtained (Chen *et al.,* 2000)). This allows for the determination of turbulence intensities (I_{uu}, I_{vv}, I_{ww}, I_{uvw}) and Reynolds stresses ($\langle u_x^{r+2} \rangle$, $\langle u_y^{r+2} \rangle$, $\langle u_z^{r+2} \rangle$, $\langle u_x^{r*} u_y^{r*} \rangle$, $\langle u_x^{r*} u_z^{r*} \rangle$, $\langle u_y^{r*} u_z^{r*} \rangle$). The probe has a frequency response capability of up to 2 Hz and can measure velocities in the range of 2 m/s to 100 m/s, to an accuracy of ±0.5 m/s and ±1 ° of pitch and yaw for turbulence intensities below 30 %. The cobra probe design enables velocity vectors to be measured within a cone 45 ° from the axis of the probe, thus it is incapable of measuring reversed flow. The cobra probe was used to obtain boundary layer profiles at the trailing edge of the vehicle in the symmetry plane at (X, Y, Z) = (0, 0, H) and on the side of the base at (X, Y, Z) = (0, 0.5 W, 0.5 H). The probe was also traversed in planes parallel to the base of the vehicle at Z = 1 W & 2 W. Wake flow measurements were taken for 15 seconds at a sampling rate of 2,000 Hz.

Pressure measurements were taken using a multi-channel differential Dynamic Pressure Measurement System (DPMS). The DPMS comprises of two 64 channel modules, one with a full-scale measurement range of ±3.0 kPa and one with ±7.0 kPa. Each module consist of 64 channels that can be synced. The manufacturer claimed accuracy of these units is ±0.1 % of full scale output. The system was calibrated in house using a Betz manometer as a reference.

Surface pressure measurements were taken on the rear face of the model by connecting 500 mm long 1.2 mm diameter PVC tubes to the DPMS. The taps were arranged in a 7 × 7 array with span-wise and vertical spacings of 0.16 W and 0.17 W respectively (Figure 2 (a)). Measurements were taken for 60 seconds at a sampling rate of 1,000 Hz. Although the DPMS is capable of sampling at frequencies up to 1,000 Hz in practice the maximum frequency that can be resolved is limited by the response characteristics of tube system connecting the DPMS to the surface measurement location. In order to account for distortion to the time varying pressure signal, an inverse transfer function correction is used. For the setups detailed below this allowed accurate determination of frequencies up to the Nyquist frequency of 500 Hz.

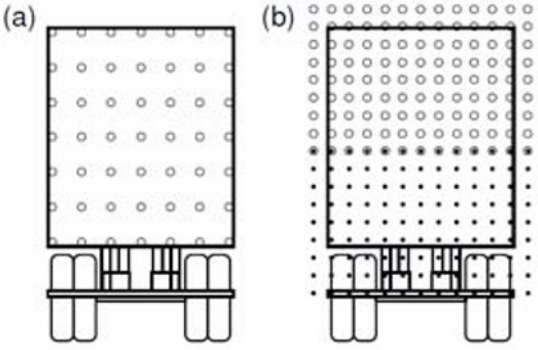

Figure 2. Schematic of (a) base pressure tap, and (b) total pressure grid locations. Probe locations for the upper (○) and lower (●) total pressure grids.

In order to obtain simultaneous data across a large spatial region in the wake, a 13 × 9 rectangular grid of forward-facing tubes was used with spacing equal to 0.096 W. The quantity measured by this device is the stream-wise component of total pressure ($p + \frac{\rho u^2}{2}$). As these tubes are forward facing, they can only obtain reliable data for flow incidence angles within a cone of acceptance before separation effects begin to dominate. (Bell, 2015) yawed a grid of total pressure probes through -20 ° to 45 °, showing that for incidence angle magnitudes up to 16 ° the measured velocity agreed with the true velocity component. Beyond ±16 ° the probe measurements dropped off more quickly than the true component of dynamic pressure. The grid was placed at two heights (Z = 225 mm to 855 mm and Z = 855 mm to 1495 mm) to capture the upper and lower regions of the wake. Figure 2 (b) shows the total pressure grid measurement locations in relation to the base of the vehicle. The probes were connected to the DPMS via 2200 mm long, 1.5 mm diameter PVC tubing, resulting in a maximum resolvable frequency of 500 Hz. Measurements were taken for 60 seconds at a sampling rate of 1,000 Hz. The grid was placed at stream-wise locations of X = 1 W, 2 W & 3 W. Base pressure measurements conducted with the lower grid positioned at each of these stream-wise positions showed a maximum change in the mean base pressure coefficient of $\Delta CP \approx 0{:}015$. For spacings of X = 2 W & X =3 W the structure of the base pressure profile remained unchanged, indicating that the wake structure was not modified significantly by the addition of the grid.

3. RESULTS

3.1. Boundary Layers

We begin our discussion of wind tunnel test results by characterising the boundary layer immediately prior to the location at which flow separates from the trailing edge of the trailer for the various heavy vehicle geometries. The boundary layer that develops along the top and sides of the trailer is the intermediary between the flow fields at the front and rear of the vehicle.

Figure 3 shows the boundary-layer profiles for both U^*

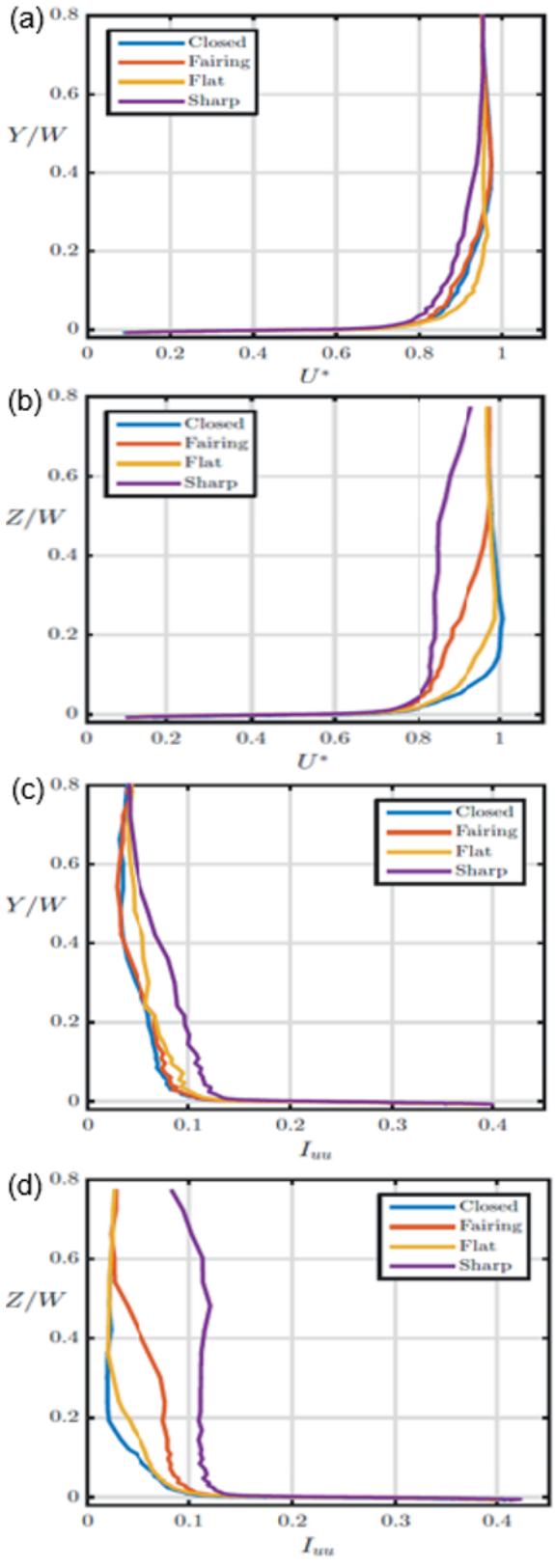

Figure 3. Detailed vehicle roof (a) and side (b) boundary layer velocity profiles and roof (c) and side (d) stream-wise turbulence intensity profiles.

and I_{uu} in the vehicle's centreline just upstream of the upper trailing edge. The Closed, Fairing and Sharp vehicles have similarly shaped velocity and turbulence profiles of differing thickness. The boundary layer of the Flat vehicle is noticeably thinner than that of the lower drag Fairing vehicle. This is attributed to the acceleration of flow over the rounded leading edges of the trailer, while the roof fairing deflects high-speed flow above the trailer, leading to lower near-wall velocities. The Sharp vehicle produces a significantly different boundary layer profile due to flow separation over the trailer leading edges. The profiles approximate those of a thin boundary layer approaching a constant reduced effective free-stream velocity over the range of $0.1 < Z = W < 0.5$, after which the profiles begin trending towards true free-stream values.

Boundary layers measured at the trailing edge on the side of the vehicle, at the half height point of the box trailer show more subtle differences between the configurations.

This is a result of the prime mover having a similar width to the trailer compared to the height. Figure 3 shows that the Sharp cab once again has the greatest velocity deficit and turbulence levels, although it now follows a more conventionally shaped profile, similar to the other configurations.

The range of boundary layer profiles across a typical heavy vehicles fleet has implications for developing both passive and active base-drag reduction technologies. For instance, variation in the state of the boundary layer is a likely explanation for the spread in optimal boat-tail angle reported in the literature (Burton *et al.*, 2013), as the boundary-layer shape and thickness determine its ability to overcome the adverse pressure gradient imposed by the angled diffusing surface.

3.2. Base Pressure

Contours of mean base pressure for the Closed-Skirts, Closed, Fairing, Flat and Sharp vehicles are presented in order of increasing drag coefficient in Figure 4. All configurations show a similar time-averaged pressure distribution, with a band of low pressure across the lower region of the base, highest pressure at the top and a larger magnitude pressure gradient in the vertical direction than the horizontal one. These features are consistent with the wake structure of simplified heavy vehicle models such as the Ground Transportation System (McArthur *et al.*, 2016), where the low pressure region is associated with the proximity of the main lower vortex. Also apparent over the upper region of the base are two vertical regions of slightly lower pressure around $Y \approx 0.4$ W, possibly an indication of the signature of the vertical arms of a time-averaged toroidal vortex.

Figure 5 shows an approximately positive linear trend between the change in drag and base pressure for the Closed, Fairing, Flat and Sharp configurations. The primary geometric differences between these configurations concern

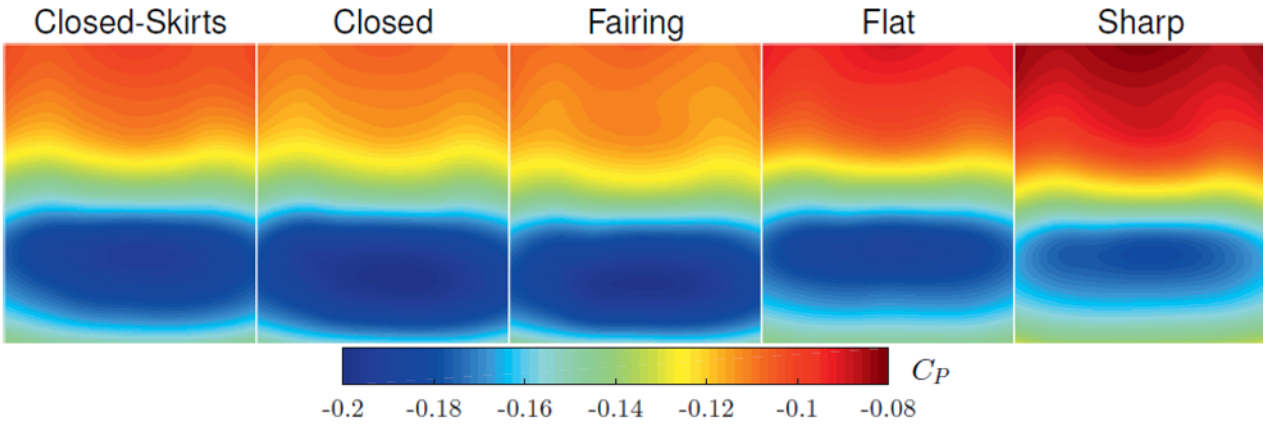

Figure 4. Detailed vehicle mean base pressure.

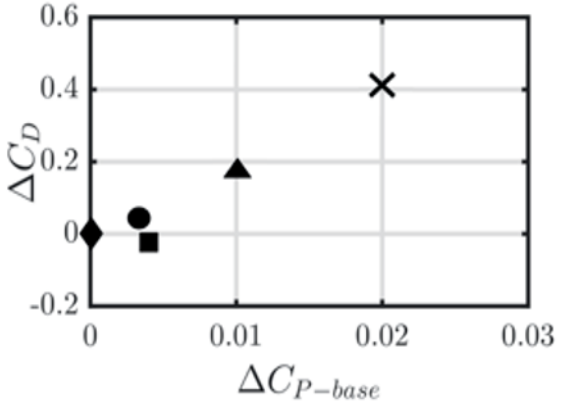

Figure 5. Change in base pressure coefficient vs change in drag coefficient, referenced to the ♦ Closed model for ● Fairing, ▲Flat, X Sharp and ■ Closed-Skirts configurations.

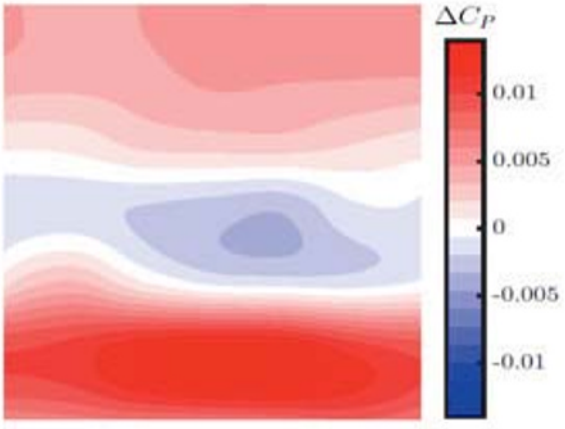

Figure 6. Base pressure difference between the Closed-Skirts and Closed configurations.

the transition of flow between the tractor and trailer, which has been shown to govern the boundary-layer development over the top and sides of the vehicle (Figure 3). The increased base pressure for higher-drag cases is a result of thicker boundary layers along the sides providing a buffer between the wake and free-stream flow, thus reducing the entrainment rate of high-speed flow. This result is consistent with the simplified, square-back bluff-body literature (Van Raemdonck *et al.*, 2009). These findings imply that there is a certain value of fore-body drag, beyond which any further reduction in fore-body drag, will modify the side boundary layers in such a way that there will be a larger increase in suction on the rear surface, resulting in a net overall drag increase. Figure 5 shows that the change in total drag is an order of magnitude larger than the change in base drag, indicating that the current class of cab-over vehicles are well within the range where fore-body drag reduction can be beneficial. This result also suggests that there is greater potential for base-drag reduction on vehicles with streamlined front ends, both in percentage and absolute terms.

A different trend is observed with the addition of side-skirts to the Closed model. This modification led to a reduction in drag and an increase in base pressure. This shows that side-skirts reduce drag not only locally on bluff under-body components, but also by increasing pressure downstream which feeds into the wake. The lower region of the base pressure is most strongly affected by the change in under-body flow. This is demonstrated in Figure 6, which shows a contour map of the base pressure difference between Closed and Closed-Skirts configurations. A band of increased pressure spanning the lower region of the base is observed for the Closed-Skirt model. Above this is a small region of slightly reduced pressure, before the Closed-Skirt model pressure is increased again on the upper region of the base. This change in base pressure distribution is indicative of an increased local pressure in the region beneath the vehicle. The higher pressure at the bottom and

lower pressure in the centre of the base is also consistent with the core of the main lower vortex being displaced upwards.

3.3. Flow Mapping

Flow mapping was conducted with the Cobra-probe on 4 configurations: Closed-Skirts, Fairing, Flat and Boat-Tails, in planes parallel to the base of the vehicle, located 1 W and 2 W downstream. Contours of these measurements are presented for probe data sampled over one half of the vehicles wake and mirrored across the vehicle centreline to obtain the full flow field. Measurements spanning the entire width of the wake for all configurations showed that steady and unsteady findings are symmetric across the width of the wake. Mean velocity components in the Y Z plane at 1 W downstream of the base are presented in Figure 7. Areas of the wake falling outside the measurement capabilities of the Cobra-probe are coloured grey. Although a large amount of the central region of the wake is not measurable insight into the mean wake behaviour can still be gained from studying the outer regions of the wake.

The Closed-Skirts, Fairing and Flat vehicles all have similarly shaped wakes, with a large regions of stream-wise velocity deficit behind the upper part of the base, which narrows as it approaches the ground. The in-plane velocity components show the flow converging towards the wake, with the inward components of the u_y appearing stronger towards the lower part of the wake. The increased stream-wise and span-wise velocity in the lower borders of the wake result from increased acceleration of the flow

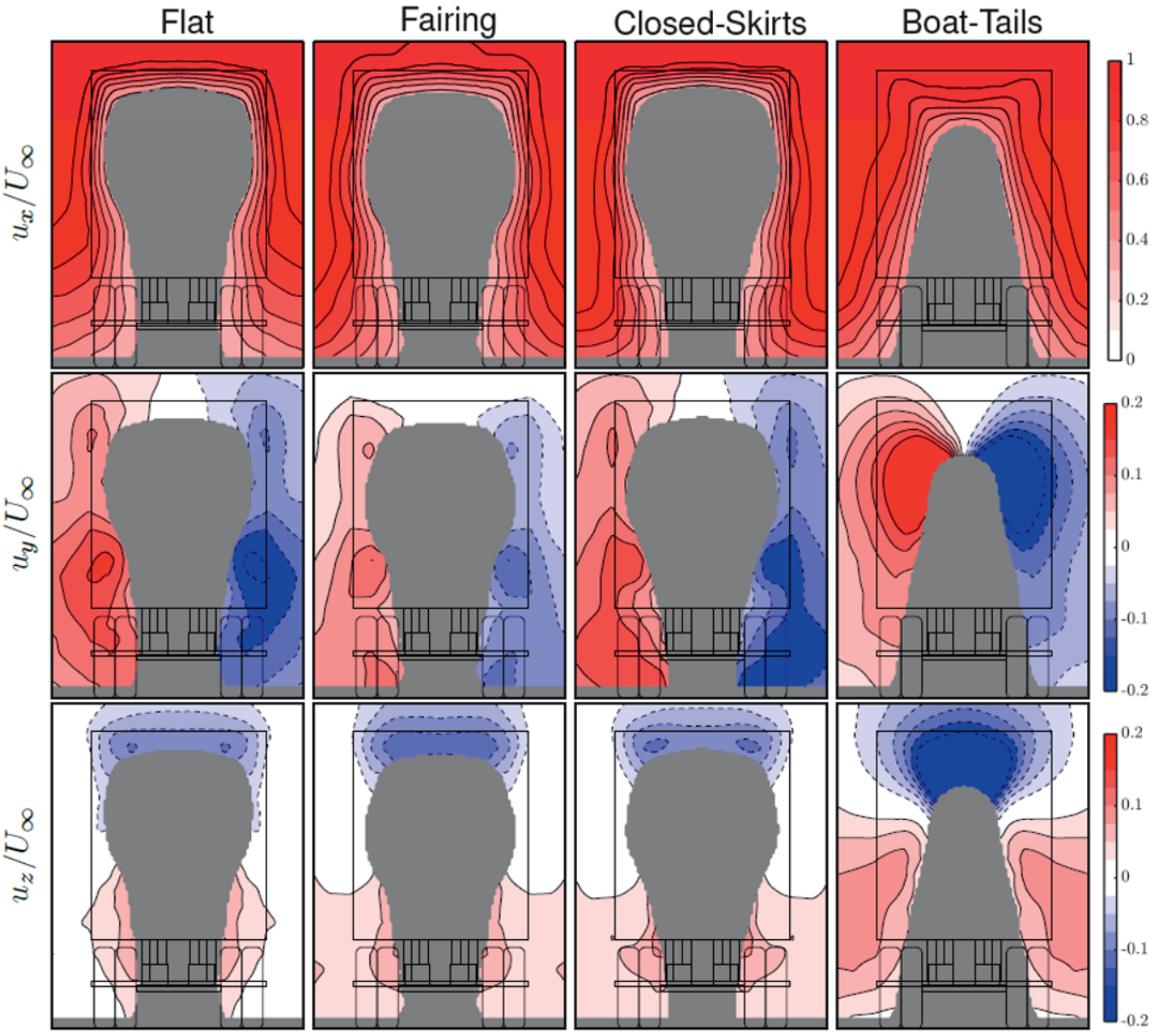

Figure 7. Mean velocity components, X = 1 W.

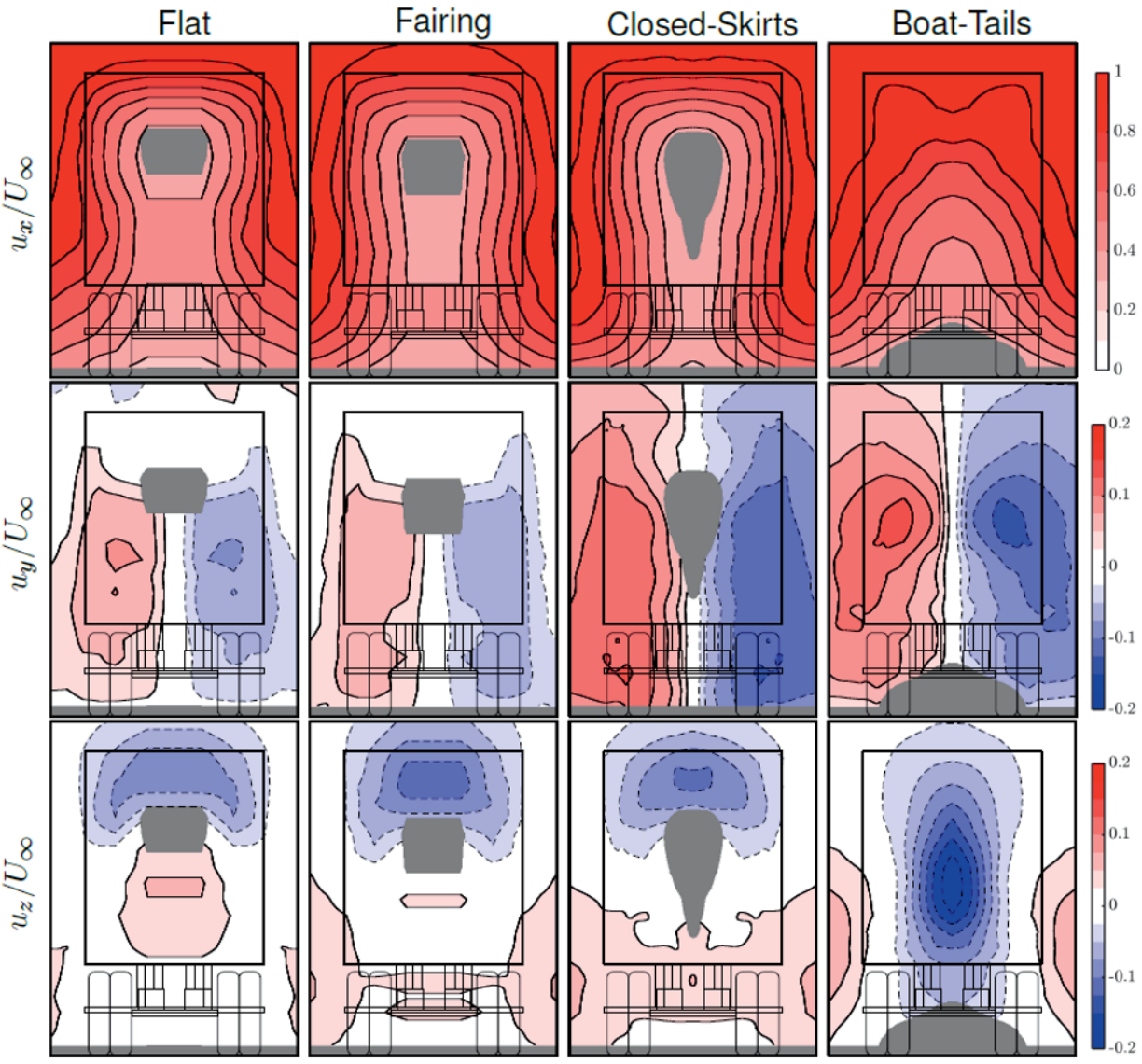

Figure 8. Mean velocity components, X = 2 W.

towards the low pressure region associated with the main lower vortex. The Closed-Skirts vehicle in particular has a strong u_y component in the lower region of the wake behind the wheels. This appears to be a result of the side-skirts reducing upstream losses along the side of the under-body. In contrast to these vehicle geometries the wake of the Boat-Tail vehicle is significantly different. For this case the stream-wise velocity deficit over the upper region of the wake is reduced and the magnitude of the in-plane velocity components increases at the upper borders of the recirculation region.

At 2 W downstream, Figure 8 shows that the u_x component for the flat-back vehicles continues to exhibit a narrowing, in line with the lower part of the base. The stream-wise velocity deficit for the Closed-Skirts case is concentrated around the centreline and the in-plane gradients are relatively high. The Fairing and Flat wakes, on the other hand have a smaller region of low u_x, and smaller in-plane gradients towards the freestream flow. This difference occurs due to the thinner low u_x, and smaller in-plane gradients towards the free-boundary layers on the Closed-Skirts model, allowing increased mixing of high-speed flow into the wake. Once again, the Boat-Tail wake shows significant differences. The size of the momentum deficit region is reduced and occurs low in the wake towards the ground plane. A central region of relatively high velocity flow directed down the centreline of the model is also apparent.

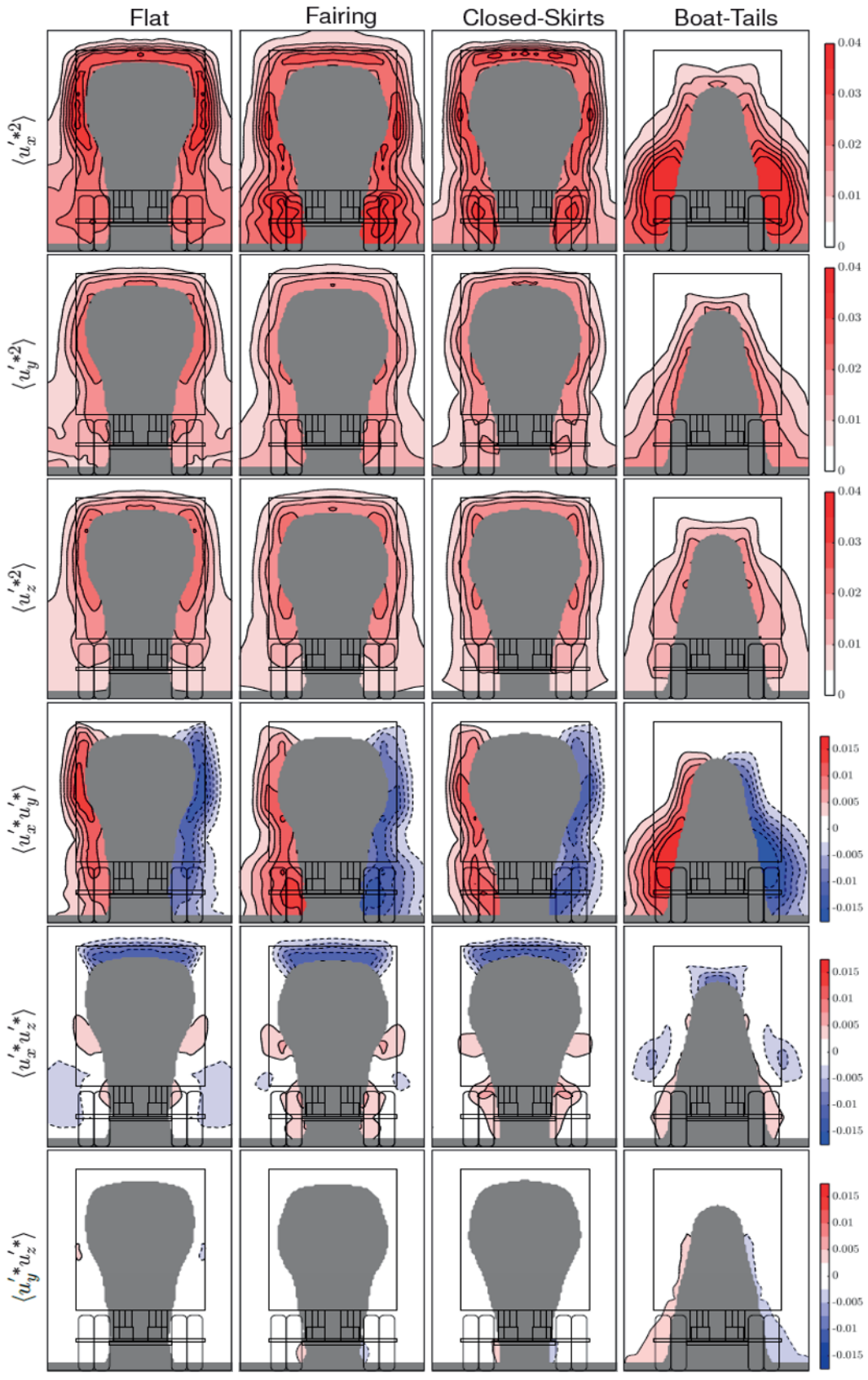

Figure 9. Reynolds stresses, X = 1 W.

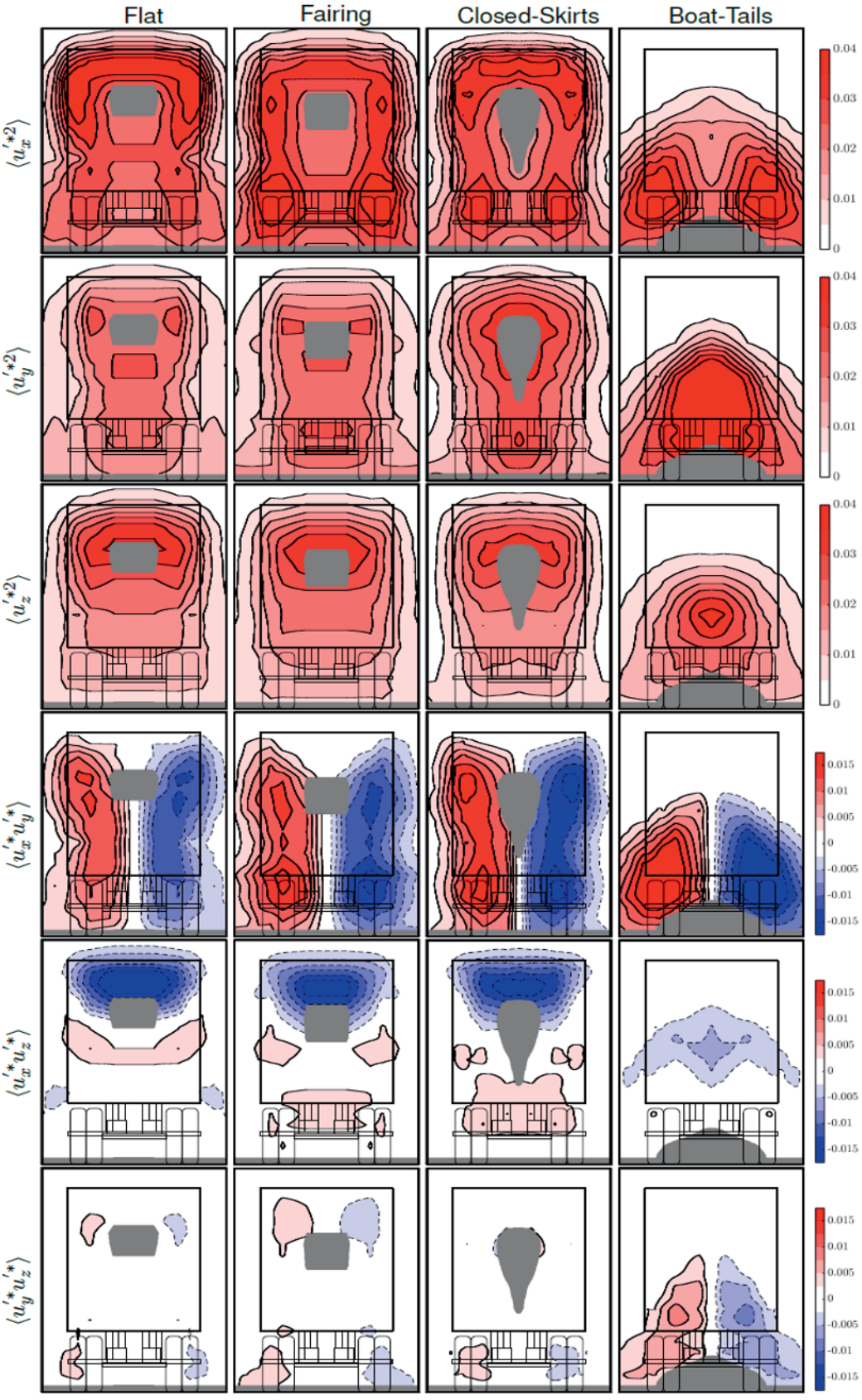

Figure 10. Reynolds stresses, X = 2 W.

Contours of the mean Normal and Shear Reynolds stresses at X = 1 W are presented in Figure 9. The Closed-Skirts, Fairing and Flat fields exhibit a number of similarities to the distribution of fluctuating velocities in the wake of the GTS as shown in (McArthur *et al*., 2016). The strongest fluctuating component is $\langle u_x^{r+2} \rangle$, which is distributed in an arch around the top and sides of the wake. For the detailed case though, strong regions of $\langle u_x^{r+2} \rangle$ extend down to the lower region of the wake, behind the wheels. This is particularly evident for the Closed-Skirts and Fairing cases. The sign and distribution of the out-of-plane shear components, $\langle u_x^{r*} u_y^{r*} \rangle$ and $\langle u_x^{r*} u_z^{r*} \rangle$, once again confirm that positive streamwise fluctuations are correlated with an increase in velocity inwards towards the centre of the wake. The in-plane Reynolds Shear $\langle u_y^{r*} u_z^{r*} \rangle$, is negligible within the measurable region of the plane. In the upper region of the wake, the Boat-Tails configuration has reduced intensity of all Reynolds-stress components. There are however, particularly large regions of elevated $\langle u_x^{r+2} \rangle$ and $\langle u_x^{r*} u_y^{r*} \rangle$ at the sides of the lower wake, which are larger and more intense than those on any of the flat-back models.

Figure 10 shows that further downstream at X = 2 W the $\langle u_x^{r+2} \rangle$, $\langle u_x^{r*} u_y^{r*} \rangle$ and $\langle u_x^{r*} u_z^{r*} \rangle$ distributions continue to increase in the upper and side shear layers as well as downstream of the wheels. The persistence of this pattern is most apparent for the Closed-Skirts vehicle. Distributions of $\langle u_y^{r+2} \rangle$ and $\langle u_y^{r*} u_z^{r*} \rangle$ are concentrated near the minima of streamwise velocity from Figure 8. Fluctuating components of the Boat-Tail wake are once again confined to the lower region of the wake. The span-wise components $\langle u_y^{r+2} \rangle$ and $\langle u_x^{r*} u_y^{r*} \rangle$ significantly outweigh the vertical components $\langle u_z^{r+2} \rangle$ and $\langle u_x^{r*} u_z^{r*} \rangle$, suggesting that the dominant fluctuations are in the span-wise direction.

3.4. Unsteady Results

Figure 11 displays power spectra of the stream-wise velocity u_x obtained at X = 2 W, surrounding contours of Figure 11 displays power spectra of the stream-wise velocity u_x obtained at X = 2 W, surrounding contours of $\langle u_x^{r+2} \rangle$, with markers showing the corresponding

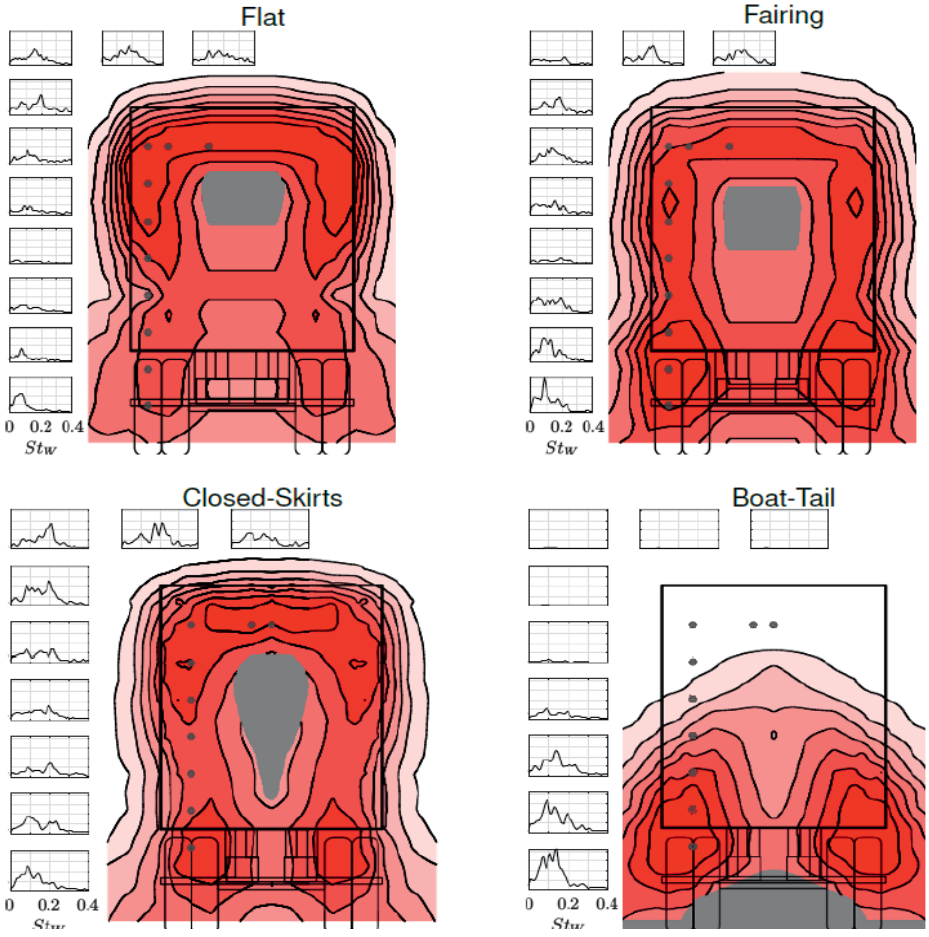

Figure 11. Contours of $\langle u_x^{r+2} \rangle$ with markers showing the spatial locations of the surrounding stream-wise velocity power-spectra plots. Probe positioned at, X = 2 W.

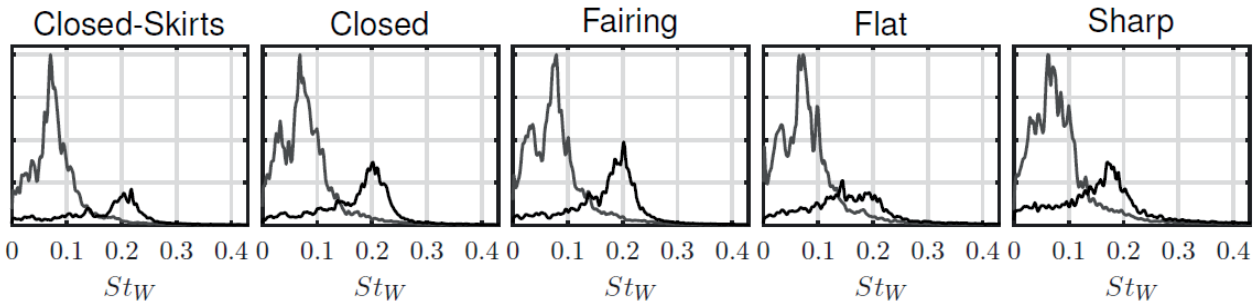

Figure 12. Detailed vehicle base-pressure power spectra, Black: $C_{P_{L-R}}$, Grey: $C_{P_{base}}$.

measurement locations for each individual spectrum. Power spectra are presented for pertinent points in the flow-field. Beginning with the Closed-Skirts case, different dominant frequencies can be seen in different regions of the wake. The upper sides of the wake show dominant frequencies at a Strouhal number ($St_W = f \cdot W/U$) of approximately $St_W \approx 0.2$. This is consistent with the frequency associated with von Kármán-like vortex shedding. This frequency is still apparent towards the lower regions of the wake, although at reduced intensity. The lower regions of high $\langle u_x^{r+2} \rangle$, however, are dominated by lower frequency content with peaks at $St_W \approx 0.09$. This indicates that the fluctuations in the lower region of the wake are associated with a different flow structure to those in the upper wake. The higher drag cases, Fairing and Flat, also have fluctuations at $St_W \approx 0.2$ in the upper region of the wake, but this does not appear to extend as far downwards into the lower regions of the wake. Additionally, the low frequency pulsations in the lower region of the Flat vehicle wake have significantly reduced power when compared to the Closed-Skirts and Fairing models. As shown before, the addition of boat-tails significantly alters the structure of the wake. Low frequency oscillations downstream of the wheels are particularly strong, while the upper wake has become steady.

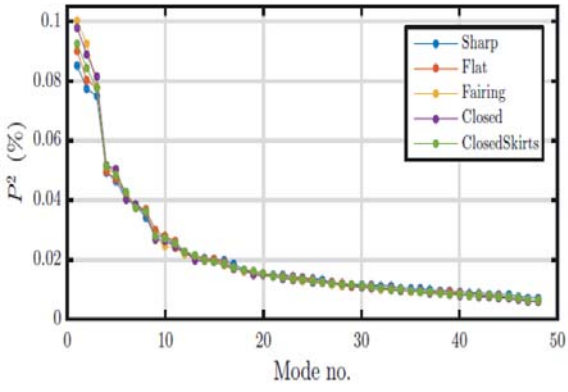

Figure 13. Base pressure POD mode rankings.

The simultaneous surface pressure measurements across the entire base of the vehicle enables the large-scale unsteady wake motions to be further characterised through their correlated surface pressure signature. Bulk changes in the wake recirculation-bubble size are inferred from the time varying, spatial average of the base pressures $C_{P_{base}}$. This is equivalent to the fluctuating component of vehicle base drag. Lateral oscillations in the wake are identified from the difference between pressures averaged over the left and right halves of the base, $C_{P_{L-K}}$.

Figure 12 contains power spectra of $C_{P_{base}}$ and $C_{P_{L-K}}$. for 5 different vehicle configurations. All $C_{P_{base}}$ spectra have a dominant peak in the range $0.062 \leq St_W \leq 0.079$. This corresponds to the wake-pumping mode, identified for the GTS in (McArthur *et al.,* 2016) and seen on other generic bodies by (Volpe *et al.,* 2014) and Duell and George, 1999), although it has not previously been reported on fully detailed heavy vehicles. For each successive higher-drag case, this peak frequency appears less dominant over the surrounding noise. The Closed, Fairing and Flat vehicles also display a second low-frequency peak at $0.032 \leq St_W \leq 0.036$. The Sharp vehicle contains elevated energy in this frequency range without a discernible peak, while the Closed-Skirts model on the other hand contains relatively lower energy in the frequency range. This leads to the supposition that low-frequency oscillations are generated in the vehicle's detailed under-body when it is exposed to the external flow-field. Point measurements comparing the spectra with and without side-skirts at a number of points along the centreline of the base show that while both configurations contain evidence of peaks at both $St_W \approx 0.03$ and 0.07, the addition of side-skirts causes a redistribution of energy from the lower-frequency peak to the higher-frequency one.

Power spectra of $C_{P_{L-K}}$ show that the dominant peak in span-wise oscillations of the wake is in the region of $St_W \approx 0.2$, suggesting that the analogy of von Kármán shedding occurs between the sides of the vehicle. In general, the peak frequency reduces with increasing drag, from $St_W \approx 0.22$ for the Closed-Skirts model to $St_W \approx 0.17$ for the Sharp model.

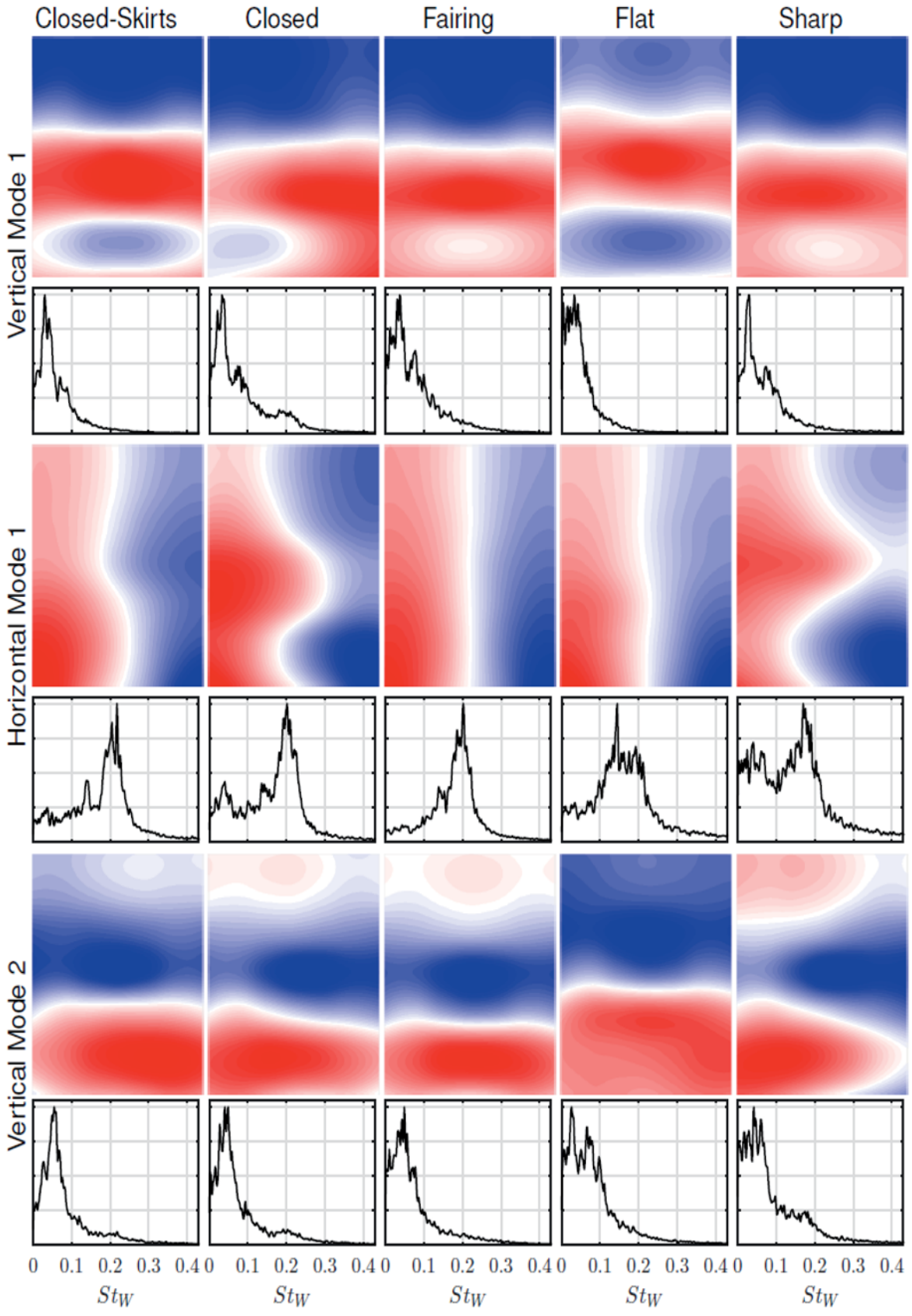

Figure 14. Base-pressure POD modes 1-3.

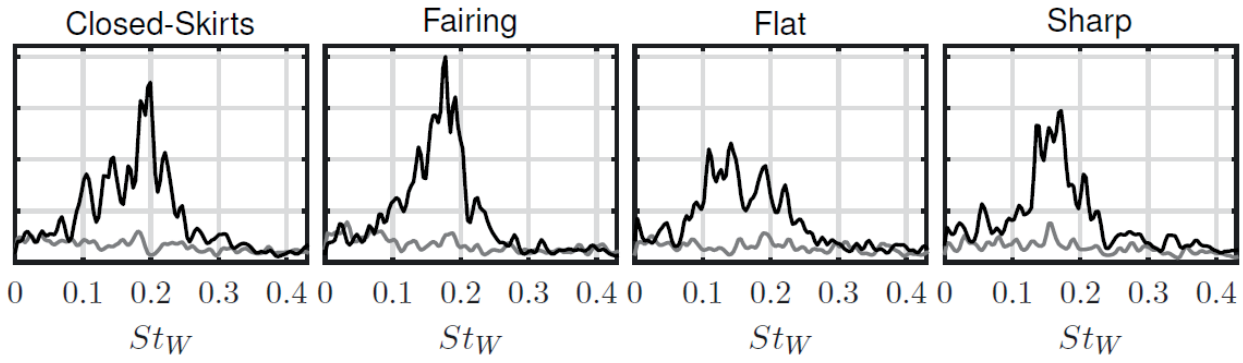

Figure 15. Power spectra of the wake barycentre location from upper total-pressure grid, X = 3 W. Black: y position, Grey: z position. Signals normalised by Fairing peak frequency.

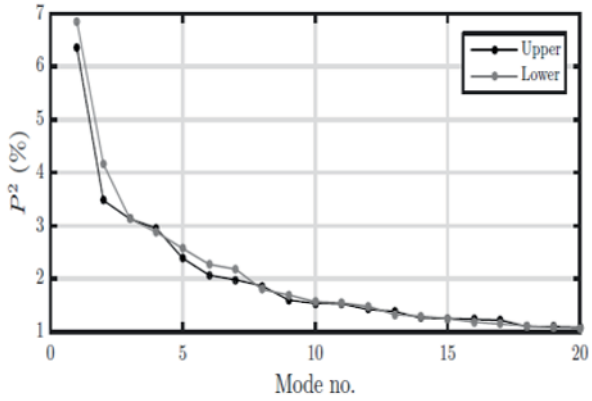

Figure 16. Total pressure POD mode rankings, X=3 W.

This is directionally consistent with the universal Strouhal number theory of (Roshko, 1955). The notable divergence from this trend is the Flat vehicle, which has increased energy levels in the range of $0.12 \leq St_W \leq 0.22$, without a dominant peak aside from a small one a at $St_W = 0.14$.

To obtain a deeper understanding of the near-wake fluctuations, a Proper Orthogonal Decomposition (POD) was constructed from the base pressure measurements of the Closed-Skirts, Closed, Fairing, Flat and Sharp configurations. Proper Orthogonal Decomposition is a modal decomposition technique proposed by (Lumley, 1967) that can isolate the dominant fluctuations in a data set by extracting the successive spatial modes which minimise the variance of all remaining elements. A review of the derivation and implementation of POD for turbulent flows can be found in (Berkooz *et al.*, 1993). The modal energy rankings (excluding Mode 0) are presented in Figure 13. Each configuration has 3 dominant modes that each account for between 7.5 and 10 % of the fluctuating content, with the following modes trailing off from around 5 %. Mode shapes and power spectra for the 3 dominant modes are presented in Figure 14. Mode 0 has been omitted from this figure as its structure is equivalent to the mean pressure contours in Figure 4, and its spectrum agrees well with the signal of $C_{P_{base}}$ in Figure 12. Mode 1 is labelled below as Vertical Mode 1, as its spatial distribution varies mainly in the vertical direction. For this mode the Closed-Skirts, Closed, Fairing and Sharp vehicles have similar spatial distributions, with an upper and lower band being 180 ° out of phase about $Z/H \approx 0.6$. These modes have a spectral peak at $St_W = 0.03$ and a secondary peak at $St_W = 0.08$, corresponding to the secondary and dominant frequencies of the mean base pressure presented in Figure 12. The Closed Vertical Mode 1 shows signs of asymmetry as well as a slight bump in the mode spectrum at $St_W \leq 0.2$, suggesting that the von Kármán-like shedding is interacting with this mode. Flat Mode 1 differs from the others, both spatially by being phase shifted vertically, and containing no distinct spectral peak.

Vertical Mode 2 contains the final dominant base pressure mode. The spatial distributions are of similar wavelength to those in Vertical Mode 1, although phase shifted. The mode structure for the Closed-Skirts, Closed and Fairing models has out-of-phase bands at $Z/H = 0.15$ and $Z/H = 0.55$, and fluctuate at dominant frequencies of $St_W = 0.054$, 0.049 and 0.049, respectively. The location and structure of this mode are consistent with the expected pressure fluctuations associated with a vertical oscillation in the position of the main lower vortex core. The Sharp configuration has a similarly shaped, but less symmetric mode with no dominant frequency. Once again, Vertical Mode 2 for the Flat model differs from the other configurations, both in terms of mode shape and spectra.

The base pressure POD modes point to a striking similarity in the dominant unsteady flow physics between the Closed-Skirts, Closed, Fairing and Sharp vehicles. This is despite the large range of drag coefficients which varies $\Delta CD \approx 0.4$ between these configurations. It is interesting to note that the Flat vehicle, which has drag and mean base-pressure values in between those of the Sharp and Fairing vehicles, suffers from a significant loss of coherence in the dominant fluctuations as well as a change

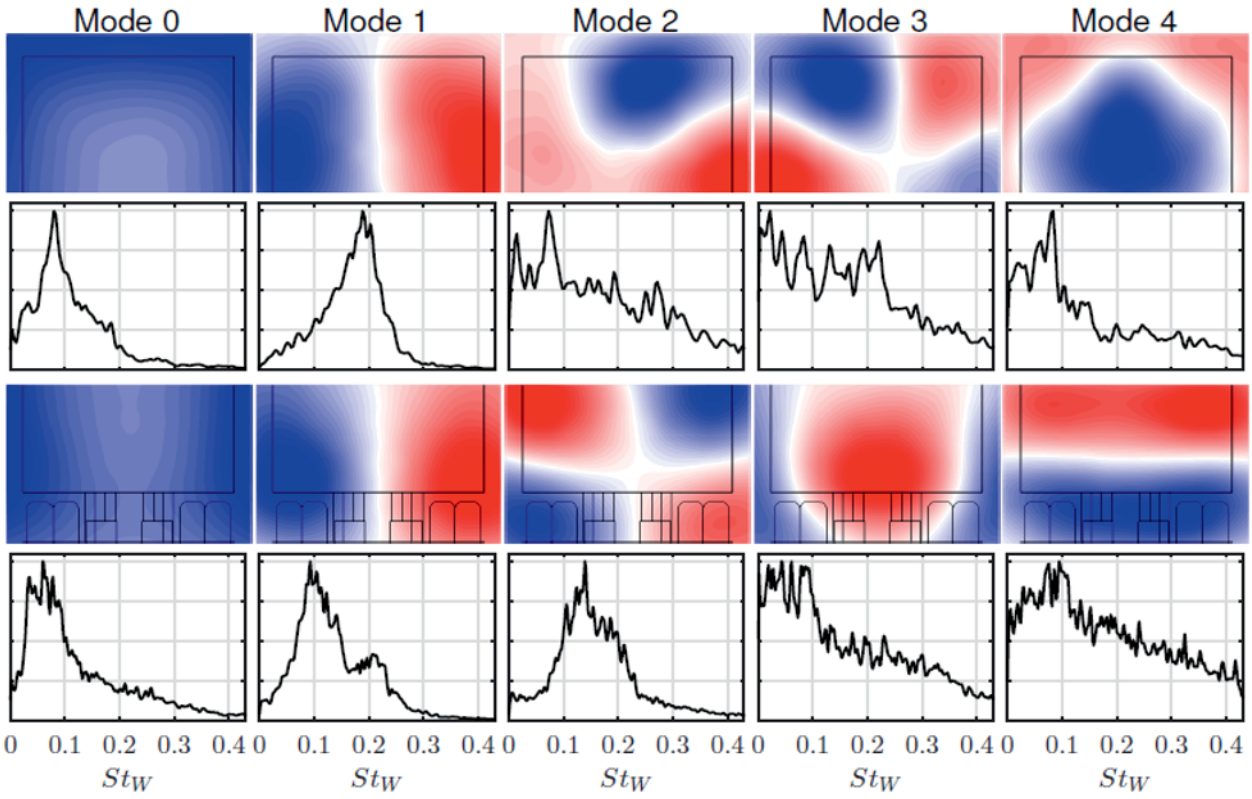

Figure 17. Fairing vehicle total pressure POD modes 0-4.

to the structure of the primary vertical modes. A possible cause of this is the interference from flow stuctures generated over the roof of the flat top tractor, which is not apparent in the Closed or Fairing configuration and would not be expected to survive past the front of the trailer for the Sharp configuration.

The unsteady flow physics associated with each of the vehicle configurations is further detailed through analysis of the upper and lower wake pressures measured using the total pressure grid. The global wake dynamics is first characterised through the time varying nature of the location of the wake total pressure barycenter, (see Varon *et al*., 2017 for further details on this method). In this study the pressure barycenter has been derived from instantaneous stream-wise total pressure fields measured using the grid in the upper wake position at a stream-wise location of X = 3 W. Power spectra of the Y and Z coordinates marking the location of the wake total pressure field barycenter are presented in Figure 15. The Closed-Skirts and Fairing models both show dominant peaks in the span-wise direction at, or just under $St_W = 0.2$, while for the Flat and Sharp models these peaks occur at a lower frequency and are spread across a wider frequency band. Once again the Flat signal shows a less defined dominant frequency than the higher drag Sharp configuration. This result agrees with the base pressure measurements in Figure 12, confirming the loss of periodicity of the von Kármán-like shedding behind the Flat vehicle.

Further insight into these spectra is gained through a Proper Orthogonal Decomposition of the $C_{\left\{P_{Static}+\frac{1}{2}\rho u^2\right\}}$ fields obtained from the total pressure grid. Here for brevity only the POD modal analysis is presented for the Fairing configuration. Figure 16 below shows the distribution of fluctuating energy amongst the first 20 modes in the plane 3 W behind the Fairing cab for both the upper and lower grid positions. Both follow similar trends, with Mode 1 accounting for around 6.5 % of the energy, with a jump down to Mode 2 with 3.5 ~ 4.1 %, before a gradual drop-off for the remaining modes.

The decomposition of pressure fields for the upper region of the wake (Figure 17) shows 2 modes with coherent frequency peaks. Mode 0, the mean mode contains a peak frequency of $St_W = 0.08$, corresponding to the wake pumping frequency and Mode 1 peaks at $St_W = 0.2$, showing the von Kármán-like oscillation as the only other coherent structure to have survived 3W downstream of the vehicle's base. In the lower half of the wake, modes 0, 1 and 2 each contain discrete spectral content. Mode 1, which is structurally equivalent to the von Kármán mode above, has a main spectral peak at $St_W = 0.1$ and a secondary peak at $St_W = 0.2$. Mode 2 divides the flow-field into 4 quarters, with the upper-left and lower-right corners being 180°

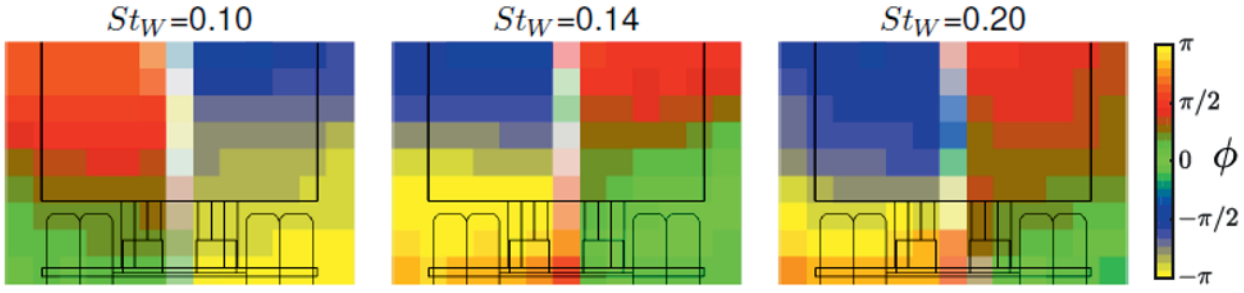

Figure 18. Fairing vehicle total pressure phase relationship. Measurement location: X = 3 W.

out-of-phase relative to the lower-left and upper-right. This mode has raised energy levels across $0.1 \leq St_W \leq 0.2$, with a peak at $St_W = 0.14$.out-of-phase relative to the lower-left and upper-right. This mode has raised energy levels across $0.1 \leq St_W \leq 0.2$, with a peak at $St_W = 0.14$.

To better understand the physical interpretation of Modes 1 & 2 in the lower region of the wake, phase information is obtained by simultaneously performing ffts at each grid point. Plotted below in Figure 18 are the phase relationships for the three peak frequencies of interest (StW = 0.10, 0.14 and 0.20). In each case the two sides of the wake are 180 ° out-of-phase, consistent with a span-wise oscillation. It is also apparent that the upper region of the wake leads the lower region by ≈ 90 °. This indicates that the von Kármán-like shedding in the upper art of the wake is driving the lateral oscillations in the lower wake.

4. CONCLUSION

This investigation into the aerodynamics of detailed prime-mover trailer geometries revealed how the steady and unsteady wake flow structure responds to the addition of various passive flow control devices systematically fitted to a 1:3 scale wind tunnel model. Until now the understanding of the wake flow physics of heavy vehicles has primarily been developed from simplified generic bodies and limited studies with realistic heavy vehicle geometries. The overall aerodynamic performance of the detailed test model is a function of aerodynamic flows which can be considered to originate at the front and rear portions of the vehicle. Flow control devices that reduced flow separation from frontal regions resulted in an increase in momentum in the near surface flow downstream towards the rear of the model. While a net reduction in the drag coefficient was achieved, by minimising the wake originating from the prime-mover and leading edges of the trailer, this also had the effect of increasing the base pressure drag component. This was found to primarily be a result of a lowering of pressures associated with the vehicles' large scale lower spanwise vortex. Studies performed in the wake of the test model showed minor variations in both the steady and unsteady wake structure for the model fitted with various types of fairings. This was despite the large range of drag coefficients measured between these configurations which varied $\Delta C_D \approx 0.4$. The dominant unsteady wake modes for these test cases was associated with wake pumping at $St_W \approx 0.07$ and lateral von Kármán-like shedding at $St_W \approx 0.2$. Similarities in the wake structure among test cases was not observed for the model fitted with boat-tails however, which resulted in a significant restructuring of the wake flow topology. The addition of the boat-tails resulted in the upper half of the wake becoming steady while strong low frequency oscillations were present downstream of the wheels. The variation in the steady and unsteady nature of detailed body wake flows suggest that attention should be paid to how realistic heavy vehicle geometries will impact the effectiveness of advanced flow control devices that aim to provide aerodynamic benefits above what is currently achievable.

ACKNOWLEDGEMENT–This research was supported under the Australian Research Council's Linkage Projects funding scheme (project number LP0991170).

REFERENCES

Bell, J. R. (2015). *The slipstream and wake structure of high-speed trains*. Ph.D. Dissertation. Monash University. Melbourne, Australia.

Berkooz, G., Holmes, P. J. and Lumley, J. L. (1993). The proper orthogonal decomposition in the analysis of turbulent flows. *Annual Review of Fluid Mechanics* **25, 1**, 539–575.

Burton, D., McArthur, D., Sheridan, J. and Thompson, M. (2013). Contribution of add-on components to the aerodynamic drag of a cab-over truck-trailer combination vehicle. *SAE Int. J. Commercial Vehicles* **6**, **2013-01-2428**, 477–485.

Castelain, T., Michard, M., Szmigiel, M., Chacaton, D. and Juvé, D. (2018). Identification of flow classes in the wake of a simplified truck model depending on the underbody velocity. *J. Wind Engineering and Industrial Aerodynamics*, **175**, 352–363.

Chen, J., Haynes, B. S. and Fletcher, D. F. (2000). Cobra

probe measurements of mean velocities, reynolds stresses and higher-order velocity correlations in pipe flow. *Experimental Thermal and Fluid Science* **21, 4**, 206–217.

Cooper, K. R. and Leuschen, J. (2005). Model and full-scale wind tunnel tests of second-generation aerodynamic fuel saving devices for tractor-trailers. *SAE Technical Paper No*. 2005-01-3512.

Duell, E. G. and George, A. R. (1999). Experimental study of a ground vehicle body unsteady near wake. *SAE Trans*. **108**, **6**, 1589–1602.

Haff, J. (2015). *A comparative study of engineering tools in heavy vehicle aerodynamics*. Ph.D. Dissertation. Technische Universität Ilmenau. Ilmenau, Germany.

Hooper, J. D. and Musgrove, A. R. (1997). Reynolds stress, mean velocity, and dynamic static pressure measurement by a four-hole pressure probe. *Experimental Thermal and Fluid Science* **15, 4**, 375–383.

Lanser, W., Ross, J. C. and Kaufman, A. E. (1991). Aerodynamic performance of a drag reduction device on a full-scale tractor/trailer. *SAE Trans*., 2688–3627.

Leuschen, J. and Cooper, K. R. (2006). Full-scale wind tunnel tests of production and prototype, second-generation aerodynamic drag-reducing devices for tractor-trailers. *SAE Technical Paper No*. 2006-01-3456.

Lumley, J. L. (1967). The structure of inhomogeneous turbulent flows. *Atmospheric Turbulence and Radio Wave Propagation*.

McArthur, D., Burton, D., Thompson, M. and Sheridan, J. (2016). On the near wake of a simplified heavy vehicle. *J. Fluids and Structures*, **66**, 293–314.

McArthur, D., Burton, D., Thompson, M. and Sheridan, J. (2018). An experimental characterisation of the wake of a detailed heavy vehicle in cross-wind. *J. Wind Engineering and Industrial Aerodynamics*, **175**, 364–375.

McArthur, D. J., Burton, D., Thompson, M. and Sheridan, J. (2013). Development of a wind tunnel test section for evaluation of heavy vehicle aerodynamic drag at a scale of 1:3. *SAE Int. J. Commercial Vehicles* **6, 2**, **2013-01-2455**, 522–528.

Roshko, A. (1955). On the wake and drag of bluff bodies. *J. Aeronautical Sciences* **22**, **2**, 124–132.

Van Raemdonck, G., Cojocaru, M. and Van Tooren, M. (2009). Time dependant pressure analysis of a bluff body with the aid of proper orthogonal decomposition. *14th Int. Conf. Fluid Flow Technologies.* Budapest, Hungary.

Varon, E., Eulalie, Y., Edwige, S., Gilotte, P. and Aider, J. L. (2017). Control of the chaotic dynamics of a turbulent 3D wake. *arXiv:* 1712.00416.

Volpe, R., Devinant, P. and Kourta, A. (2014). Unsteady experimental characterization of the natural wake of a squareback Ahmed model. *ASME 4th Joint US-European Fluids Engineering Division Summer Meeting collocated with the ASME 12th Int. Conf. Nanochannels, Microchannels, and Minichannels*. Chicago, IL, USA.